



NO_x storage and reduction properties of model ceria-based lean NO_x trap catalysts

Chuan Shi^{a,b}, Yaying Ji^a, Uschi M. Graham^a, Gary Jacobs^a, Mark Crocker^{a,*}, Zhaoshun Zhang^b, Yu Wang^b, Todd J. Toops^c

^a Center for Applied Energy Research, University of Kentucky, Lexington, KY 40511, USA

^b Dalian University of Technology, Dalian, China

^c Fuels, Engines, and Emissions Research Center, Oak Ridge National Laboratory, 2360 Cherahala Blvd., Knoxville, TN 37932, USA

ARTICLE INFO

Article history:

Received 11 October 2011

Received in revised form 17 February 2012

Accepted 24 February 2012

Available online 5 March 2012

Keywords:

Ceria

Barium

Lean NO_x trap catalyst

Storage

Reduction

ABSTRACT

Three kinds of model ceria-containing LNT catalysts, corresponding to Pt/Ba/CeO₂, Pt/CeO₂/Al₂O₃ and Pt/BaO/CeO₂/Al₂O₃, were prepared for comparison with a standard LNT catalyst of the Pt/BaO/Al₂O₃ type. In these catalysts ceria functioned as a NO_x storage component and/or a support material. The influence of ceria on the microstructure of the catalysts was investigated, in addition to the effect on NO_x storage capacity, regeneration behavior and catalyst performance during lean/rich cycling. The Pt/Ba/CeO₂ and Pt/BaO/CeO₂/Al₂O₃ catalysts exhibited higher NO_x storage capacity at 200 and 300 °C relative to the Pt/BaO/Al₂O₃ catalyst, although the latter displayed better storage capacity at 400 °C. Catalyst regeneration behavior at low temperature was also improved by the presence of ceria, as reflected by TPR measurements. These factors contributed to the superior NO_x storage-reduction performance exhibited by the Pt/Ba/CeO₂ and Pt/BaO/CeO₂/Al₂O₃ catalysts under cycling conditions in the temperature range 200–300 °C. Overall, Pt/BaO/CeO₂/Al₂O₃ (which displayed well balanced NO_x storage and regeneration behavior), showed the best performance, affording consistently high NO_x conversion levels in the temperature range 200–400 °C under lean-rich cycling conditions.

© 2012 Elsevier B.V. All rights reserved.

1. Introduction

Vehicular engines operating under lean burn conditions are becoming increasingly popular due to their superior fuel economy as compared to conventional Otto gasoline engines [1]. However, the toxic NO_x exhaust gas components of lean-burn engines cannot be efficiently removed with three-way catalysts which are effective only under stoichiometric conditions. Consequently, selective catalytic reduction (SCR) of NO_x using urea as a reductant has been developed for mobile lean NO_x removal [2,3]. While this technology is well suited for heavy duty diesel applications, for light duty applications lean NO_x trap (LNT) catalysts (otherwise known as NO_x adsorber or NO_x storage-reduction catalysts) appear to offer a cheaper and more practical alternative [4–6].

LNT catalysts work under cyclic conditions of fuel lean and fuel rich environments. Under lean exhaust conditions, when oxygen is in excess, NO_x is adsorbed on the catalyst; under rich conditions, when an excess of reductants is present, NO_x reduction takes place. In principle, a LNT catalyst should have sites for NO_x sorption (alkali metal or alkaline earth metal compounds) and sites for NO_x

oxidation/reduction (noble metals). Consequently, the proximity of the two active components is one of the key factors influencing LNT performance [7,8].

In addition to the above components, ceria is also an important constituent of LNTs formulated for lean burn gasoline applications. The common application of CeO₂ in three-way automotive catalysis results from the fact that ceria can act as an oxygen-storage component [9,10]. Similarly, in LNT catalysts its role is to provide the necessary oxygen storage capacity (OSC) when the engine is operating under stoichiometric conditions. In these applications the ceria is typically promoted with a noble metal such as Pt, which essentially acts as a conduit for the storage of oxygen and its consumption by reducing agents. Indeed, the strong metal–support interaction (SMSI) between noble metals and ceria has been recognized as an important factor which affects both the microstructure and redox properties of ceria-based catalysts [11,12].

In addition to providing OSC, ceria fulfills a number of other functions in LNT catalysts. Firstly, ceria has been found to be an effective support for BaO. Eberhardt et al. [13] compared the behavior of Ba/Al₂O₃ and Ba/CeO₂ materials and found that no solid/solid reaction between Ba and ceria occurred below 780 °C in air, while Ba reacted at lower temperature with Al₂O₃ to form inactive barium aluminates. Casapu et al. [14] studied LNT catalysts that contain CeO₂ as a support material and observed the formation of BaCeO₃

* Corresponding author. Tel.: +1 859 257 0295; fax: +1 859 257 0302.

E-mail address: crocker@caer.uky.edu (M. Crocker).

at 800 °C. However, decomposition of BaCeO₃ was found to occur at 300–500 °C in the presence of NO₂/H₂O or CO₂ [14,15], resulting in an improvement in NO_x storage capacity. Another recent report indicates that BaCeO₃ formation is inhibited in the presence of CO₂ at concentrations as low as 5% [16]. In comparison, BaAl₂O₄ is much more stable under typical operating conditions, although it can be converted to BaCO₃ and Al₂O₃ at room temperature in the presence of liquid water [17,18].

It has been established in a number of studies that ceria and its mixed oxides are able to store NO_x [19–24]. Furthermore, Pt/BaO/CeO₂ was reported to exhibit higher NO_x storage efficiency than Pt/BaO/Al₂O₃ at 300 °C for Ba loadings of less than ca. 10 wt% [11]. The effect of La₂O₃-stabilized ceria incorporation on the functioning of fully formulated lean NO_x trap catalysts has also been investigated [25,26]. The presence of ceria was found to be beneficial for both the NO_x storage and reduction functions of the catalyst, as well as increasing the selectivity of NO_x reduction to N₂ (rather than NH₃). Simultaneously, these ceria containing catalysts also exhibited improved properties with respect to their sulfation–desulfation behavior [27], arising from the fact that ceria is able to store sulfur in the form of sulfate, the resulting cerium sulfates being less stable than barium sulfates [27–29].

In order to better understand the role of ceria in NO_x storage and reduction, in this study model Ce-containing LNT catalysts were prepared for comparison with a standard LNT catalyst of the Pt/BaO/Al₂O₃ type. The catalysts comprised Pt/BaO/CeO₂, in which ceria functioned principally as a support material; Pt/CeO₂/Al₂O₃, in which ceria was used as the NO_x storage component; and Pt/BaO/CeO₂/Al₂O₃, in which both Ba and Ce acted as NO_x storage components. In this paper we report a study of their micro-structural properties, NO_x storage performance, reduction behavior, and catalytic properties under NO_x storage–reduction cycling.

2. Experimental

2.1. Catalyst preparation

All catalyst samples were prepared by incipient wetness impregnation. In the case of Pt/BaO/CeO₂ (hereafter denoted by the sample code PBC), CeO₂ (Rhodia, surface area of 119 m²/g) was impregnated with an aqueous solution of Ba(O₂CCH₃)₂, dried and calcined at 500 °C for 3 h in air. The Ba-loaded CeO₂ was subsequently impregnated with aqueous tetraammine platinum(II) nitrate and further calcined at 500 °C for 3 h. Pt/BaO/Al₂O₃ (PBA) was prepared similarly, using γ-Al₂O₃ (surface area of 132 m²/g) as the support. Pt/BaO/CeO₂/Al₂O₃ (PBCA) was prepared by the following method: the γ-Al₂O₃ support was impregnated with aqueous Ce(NO₃)₃, followed by drying and calcination at 500 °C in air, after which the product was impregnated with aqueous Ba(O₂CCH₃)₂, dried and calcined at 500 °C in air. The resulting solid was impregnated with aqueous tetraammine platinum(II) nitrate and was again dried and calcined at 500 °C in air. Pt/CeO₂/Al₂O₃ (PCA) was similarly prepared but with omission of the Ba(O₂CCH₃)₂ impregnation step. In addition, Pt/CeO₂ (PC) and Pt/Al₂O₃ (PA) were prepared as reference samples, via the respective impregnation of CeO₂ and Al₂O₃ with aqueous tetraammine platinum(II) nitrate, followed by drying and calcination at 500 °C. The compositions of the prepared catalysts are shown in Table 1.

2.2. Catalyst characterization

Surface area and pore volume analysis was performed according to the BET method by nitrogen adsorption at –196 °C using a Micromeritics Tri-Star system. Prior to the measurements catalyst

Table 1
Composition of prepared catalysts.

Catalyst	Catalyst code	Loading on support (wt%)		
		Pt	Ce	Ba
Pt/CeO ₂	PC	1	–	–
Pt/Al ₂ O ₃	PA	1	–	–
Pt/CeO ₂ /Al ₂ O ₃	PCA	1	25	–
Pt/BaO/Al ₂ O ₃	PBA	1	–	10
Pt/BaO/CeO ₂	PBC	1	–	10
Pt/BaO/CeO ₂ /Al ₂ O ₃	PBCA	1	25	10

samples were outgassed overnight at 160 °C under vacuum. Powder X-ray diffraction (XRD) measurements were performed on a Phillips X'Pert diffractometer using Cu Kα radiation. Pt dispersions were determined using a Micromeritics AutoChem II Analyzer by means of pulsed H₂ chemisorption at dry ice temperature (–78 °C) [26]. X-ray photoelectron spectroscopic (XPS) measurements were conducted using an Al Kα source operated at 10 kV and 15 mA. Binding energies were corrected for charging effects by referencing them to adventitious carbon (284.6 eV). High-resolution transmission electron microscopy (HR-TEM) and scanning transmission electron microscopy (STEM) investigations were conducted using a high resolution JEOL 2010F STEM outfitted with a URP pole piece, Gatan 2000 GIF, X-ray detector, GATAN DigiScan II and EmiSpec EsVision software. STEM images were acquired using a 2 Å probe. Temperature programmed reduction (TPR) experiments on the as-synthesized catalysts were performed using a Micromeritics AutoChem II Analyzer equipped with a TCD detector to monitor H₂ uptake. Samples were heated from room temperature to 600 °C at a rate of 10 °C/min under flowing 5% H₂/Ar. Prior to TPR, samples were pre-treated in Ar at 120 °C for 1 h to remove adsorbed water.

2.3. XANES/EXAFS measurements

X-ray absorption spectroscopy (XAS) on reference (Pt⁰ foil and PtO₂) and catalyst samples was conducted at Brookhaven National Laboratory (Beamline X-18b). Catalysts were reduced *in situ* in flowing H₂ at 573 K and held for ~0.5 h, prior to cooling to liquid N₂ temperatures under a H₂ flow. The beamline was equipped with a Si(111) channel cut monochromator. A crystal detuning procedure was used to remove harmonic content from the beam and make the relative response of the incident and transmission detectors more linear. The X-ray flux for the beamline was ca. 1 × 10¹⁰ photons per second at 100 mA and 2.8 GeV; the usable energy range was from 5.8 to 40 keV. EXAFS/XANES spectra were recorded in transmission mode near the Pt L_{III} edge and close to the boiling temperature of liquid nitrogen to minimize contributions to the dynamic Debye–Waller factor. Sample thickness was determined by calculating the amount in grams per square centimetre of sample (w_D) by utilizing the following thickness equation

$$w_D = \frac{\ln(I_0/I_t)}{\sum \{(m/r)_j w_j\}} \quad (1)$$

where m/r is the total cross section (absorption coefficient/density) of element “j” in the sample at the absorption edge of the EXAFS element under consideration (units, cm² g^{–1}), w_j is the weight fraction of element j in the sample and $\ln(I_0/I_t)$ was taken over a typical range of 1–2.5. Boron nitride was utilized to dilute the sample, such that the wafer could be self-supported. Smooth self-supporting pellets, free of pinholes, were pressed and loaded into the *in situ* XAS flow cell and the treatment gas was directed to the sample area. The cell was purged for an extended period with a high flow rate of He to ensure removal of air, prior to the reduction treatment. EXAFS data reduction and fitting were carried out using the WinXAS [30], Atoms [31], FEFF [32], and FEFFIT [32] programs. The k - and r -ranges

Table 2
Gas composition used for NO_x storage/reduction cycling experiments.

Parameter	Lean	Rich
Duration (s)	120	10
Temperature (°C)	200–400	200–400
Space velocity (h ⁻¹)	30,000	30,000
NO (ppm)	300	0
O ₂ (%)	8	0
H ₂ (%)	0	0.64
CO (%)	0	1.06
H ₂ O (%)	5	5
CO ₂ (%)	5	5
Ar (%)	Balance	Balance

were chosen to be 2.5–9.33 Å⁻¹ and 1.5–3.4 Å. The catalyst samples examined comprised PBA and PBCA. In the case of PBC, satisfactory data could not be obtained due to the high ceria content of the sample (ceria has a very strong absorption at the Pt L₃-edge, which interferes with the Pt signal).

2.4. NSC and NO_x-TPR experiments

NO_x storage capacity (NSC) and NO_x-TPR experiments were performed in a microreactor using a chemiluminescence NO_x analyzer and a mass spectrometer (Pfeiffer OmniStar) as the detector, respectively. Prior to both sets of measurements, the catalyst (0.15 g) was pretreated at 450 °C in flowing H₂ for 1 h. NSC measurement was then performed by exposing the catalyst to flowing gas containing 300 ppm NO, 8% O₂, 5% CO₂, 1% H₂O and balance He. TPR was performed after NO_x storage at 200 °C for 1 h in a flowing gas mixture containing 0.4% H₂, 5% CO₂, 5% H₂O and balance He. Samples were heated from room temperature to 600 °C at a rate of 10 °C/min.

2.5. Catalyst evaluation

Catalyst evaluation was performed using a quartz reactor tube loaded with ca. 150 mg of catalyst powder. Effluent gases were analyzed on-line using a mass spectrometer (SRS RGA100). All flow conditions were operated at a gas hourly space velocity (GHSV) of 30,000 h⁻¹. Before each experiment the catalyst was pretreated in 1% H₂/Ar flow at 450 °C for 1 h. NO_x storage-regeneration experiments were performed while cycling between lean and rich conditions. Following pre-treatment, the catalyst was cooled to the measurement temperature, after which lean-rich cycling was performed until the catalyst reached a cycle-average steady state. The cycling parameters and gas composition used for the cycling experiments are summarized in Table 2.

3. Results

3.1. Catalyst characterization

The results of BET surface area measurements on the prepared samples are given in Table 3. Each of the samples was calcined in air at 500 °C for 3 h before the measurements. The resulting BET data show that the specific surface areas of the support materials decreased when loaded with Ba or Ce. Accordingly, catalyst PBCA, which contains both Ba and Ce loaded on γ-Al₂O₃, possesses the lowest surface area. These decreases in surface area values with respect to the bare supports can be explained by the partial blocking or filling of the pores in the different supports.

X-ray diffractograms of PBA, PBC, PCA and PBCA are shown in Fig. 1. The characteristic reflections of Pt and PtO_x were not observed due to the low concentration of Pt in the catalyst and/or the small size of the Pt particles. Strong diffraction peaks due to

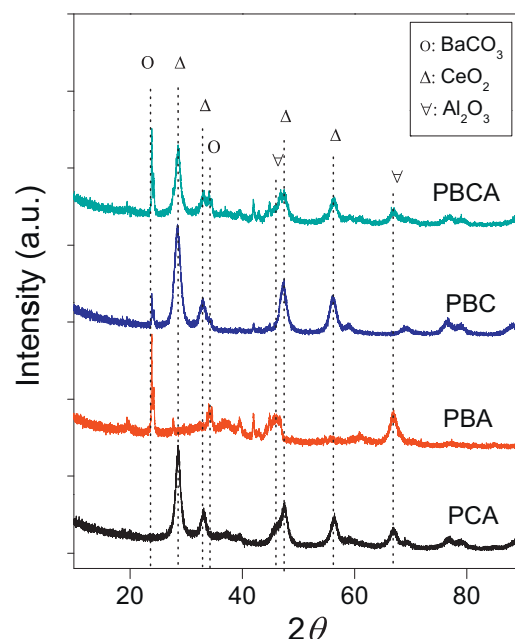


Fig. 1. XRD patterns of PCA, PBA, PBC and PBCA samples.

the cubic fluorite structure (space group Fm3m) of CeO₂ could be observed for all of the Ce-containing samples. XRD analysis confirmed the decomposition of Ba(O₂CCH₃)₂ into crystalline BaCO₃ during catalyst calcination. Crystalline BaCO₃ could be found in every Ba-containing sample, regardless of whether it was supported on γ-Al₂O₃ or CeO₂. Applying the Scherrer equation, the average BaCO₃ particle size in the Ba-containing samples was calculated based on the BaCO₃ diffraction peak at 2θ = 24°. The particle size for PBA was determined to be 65 nm, while for PBC it was 58 nm, and for PBCA it was 49 nm. These results suggest a slight improvement in the dispersion of the crystalline BaCO₃ phase when it is supported on ceria rather than on alumina, although the XRD data take no account of possible amorphous Ba phases present and therefore cannot be regarded as conclusive with respect to the Ba dispersions in the catalysts.

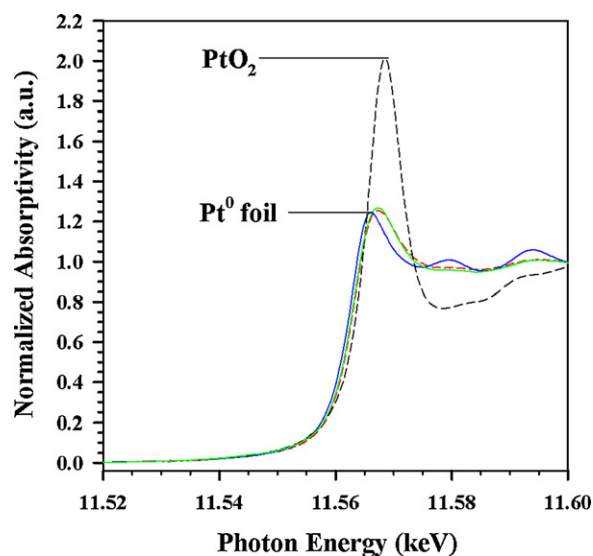


Fig. 2. Normalized XANES spectra of catalysts, including (green solid line) PBA and (red dashed line) PBCA. Reference compounds, including (blue line) Pt⁰ foil and (black dashed line) PtO₂, are also provided. (For interpretation of the references to color in this figure legend, the reader is referred to the web version of this article.)

Table 3
Physical properties of prepared catalysts and support materials.

Catalyst	Surface area (m ² /g)	Av. pore diameter (nm)	Pore volume (cm ³ /g)	Pt dispersion (%)
PBA	117	5.7	0.39	47
PBC	92	5.2	0.28	38
PCA	109	5.0	0.32	54
PBCA	93	5.3	0.30	52
Al ₂ O ₃	132	6.5	0.43	–
CeO ₂	119	6.2	0.37	–

Pt dispersions for the four samples are shown in Table 3. High Pt dispersions were obtained in all cases, the dispersion showing relatively little variation between samples. Pt dispersions in the catalysts were also examined using X-ray absorption spectroscopy. Multiple scans were taken over the catalyst samples in order to improve the signal-to-noise ratio. Nevertheless, the data for the catalyst samples were acceptable only up to a k value of 9.33 Å^{−1}. Fig. 2 shows that decreasing the k -range of the Pt⁰ foil data results in a splitting of the first coordination shell into two peaks, a larger peak followed by a smaller peak. Note that the smaller peak with its maximum position below 3.4 Å in the phase-uncorrected Fourier transform magnitude spectra is not due to second shell Pt–Pt coordination, which peaks between 3.4 and 4.1 Å. Thus, for a first shell fitting, the back-Fourier transform window was selected in a range to include the two initial peaks – those below 3.4 Å.

EXAFS spectra and results of fittings are provided in Figs. 3 and 4 and Table 4. Addition of a long Pt–O_s (*i.e.*, support bond) led to an improvement in the fitting and thus, a significant decrease in the r -factor. There is precedent for this interaction for very tiny supported Pt clusters [33]. However, the uncertainties in fitting parameters – and especially the Debye–Waller factor – for the Pt–O_s contribution were large. In addition to the much lower coordination number for the first shell Pt–Pt interaction of the catalysts, there is other evidence that the Pt clusters are very small. The XANES feature for both catalyst samples displays a broadening relative to the Pt⁰ foil. This Fano resonance feature has been discussed extensively by Koningsberger et al. [34], and is related to electron transitions into the Pt–H antibonding molecular orbital. The broadening is obvious for the two catalyst samples, but absent for the Pt⁰ foil reference, indicating that – in the case of the catalysts – a significant fraction of Pt is exposed to the surface and able to chemisorb hydrogen. Based on the average Pt coordination numbers (Table 4), the mean Pt particle size is estimated to be close to 1.5 nm in both catalysts, although the Pt clusters appear to be somewhat smaller for the Ce-containing catalyst, PBCA.

XPS measurements were also performed on the catalysts. However, due to the different support materials used, it is difficult to draw conclusions regarding the relative Ba and Pt dispersions in the catalysts. As shown in Table 5, while the Ba loading in PBC and PBA is the same (10 wt%), the atomic Ba concentration in PBC determined by XPS is much higher than that in PBA (3.01 and 1.03, respectively). Rather than proving that the Ba dispersion in PBC is higher, this can be explained by the fact that the molar mass of CeO₂ is higher than Al₂O₃, giving molar ratios of 1:26:114 for Pt:BaO:CeO₂ versus 1:26:385 for Pt:BaO:AlO_{1.5}. Additionally, the surface area of

the Al₂O₃ support (132 m²/g) is slightly higher than that of the CeO₂ support (119 m²/g). More instructive is a comparison of PBCA and PCA, since these samples contain the same CeO₂/Al₂O₃ support. Specifically, the lower ratio of Ce to Al atomic concentrations for PBCA (0.026), as compared to PCA (0.038), indicates that part of the CeO₂ in PBCA is covered by BaO. It is also noteworthy that the measured atomic Al concentrations in PBCA and PCA are virtually the same, suggesting that BaO is located mainly on the CeO₂ component, rather than on the Al₂O₃.

Information pertaining to the structure of the catalysts was also provided by electron microscopy. In the case of sample PBA, STEM images indicate that a network of randomly oriented Al₂O₃ nanorods has been overgrown by isolated barium oxide clusters or islands which are typically on the order of 10–50 nm in size and occur somewhat raised above the Al₂O₃ support. The dense barium-rich clusters can be seen in the STEM image of Fig. 5 and emerge as white regions on a light gray background that corresponds to the Al₂O₃ nanorods. The presence of BaO is further confirmed by using the 2010F X-ray detector and the analyzed spectrum (see inset) demonstrates the strong Ba-peaks for the regions identified as white dense clusters (circled in red) in the STEM image. The STEM image also includes accumulations of Al₂O₃ nanorods that are completely void of any BaO and are identified as gray areas. The Al₂O₃ nanorod surfaces play host to small Pt nanoparticles which are on average 2 nm in size and were observed to have a typical size ranging from 1.0–3.5 nm in diameter. The Pt nanoparticles can be seen as individual white regions on the gray Al₂O₃ nanorod support surfaces as shown by the STEM inset in Fig. 5. The corresponding X-ray spectrum shows both Pt peaks and Al peaks, while there is a noted absence of any Ba peaks since the analyzed region was void of Ba-rich clusters.

In the case of PBC, the nanoparticulate CeO₂ support is found typically to consist of 4–5 nm sized prismatic crystals, the narrow size distribution of the CeO₂ particles being shown in the STEM image of Fig. 6. Since barium and cerium have very similar atomic weights unlike aluminum, the STEM image does not visually distinguish the cerium and barium-rich areas as clearly as was demonstrated for the Al₂O₃-rich sample shown in Fig. 5. Some structural variation was noted mainly because of larger crystal domain sizes and the areas of interest were identified using the X-ray detector as BaO-rich zones. These are circled in color in the STEM image and one of the corresponding X-ray spectra (confirming the presence of Ba) is shown as an inset in Fig. 6. Pt nanoparticles are dispersed on the CeO₂ surfaces as demonstrated in the HR-STEM inset, these being typically 2 nm in size.

Table 4
EXAFS best fitting parameters for the average coordination numbers (N), atom distances (R), shift in E_0 , Debye–Waller factor (σ^2) and fractional misfit (r) of the Pt–O_s and Pt–Pt shells (relative uncertainties are also included) at the Pt L_{III}-edge ($\Delta k = 2.5$ – 9.33 Å^{−1}, $\Delta R = 1.5$ – 3.4 Å). S_0^2 calculated to be 0.73.

Catalyst	Pt–O _s				Pt–Pt				E_0	ΔE_0	$\sigma^2 \times 10^3$	$\Delta \sigma^2 \times 10^3$	r
	N	ΔN	R (Å)	ΔR (Å)	N	ΔN	R (Å)	ΔR (Å)					
Pt foil	–	–	–	–	12.00	Set	2.750	0.0055	6.11	0.604	1.38	0.97	0.0099
PBA	0.46	0.50	1.998	0.0385	6.81	1.40	2.724	0.0106	4.48	1.04	0.003 5.36	16.3 2.26	0.015
PBCA	0.49	0.51	2.022	0.0268	6.29	0.99	2.709	0.0086	3.41	0.843	0.005 5.37	15.1 1.77	0.0095

Note: For σ^2 and $\Delta \sigma^2$ the top value corresponds to Pt–O_s and the lower value to Pt–Pt.

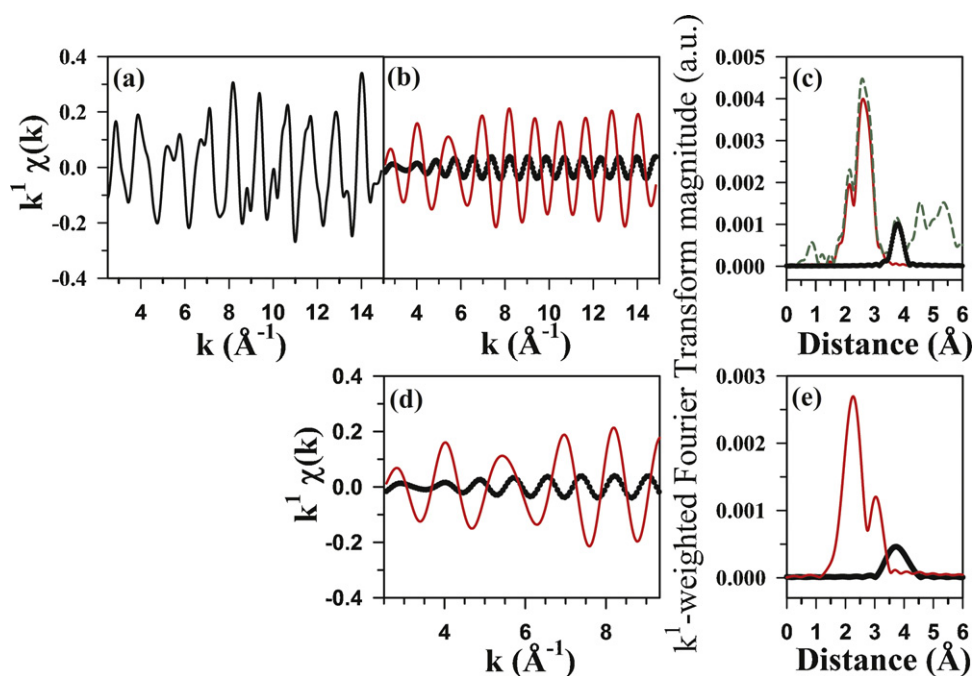


Fig. 3. EXAFS spectra of the Pt⁰ foil demonstrating the changes in the Fourier transform magnitude spectra upon shortening the k -range, including (a) the raw $k^1 \cdot \chi(k)$ spectra; (b) the filtered $k^1 \cdot \chi(k)$ versus k spectra of the (solid red) first Pt–Pt coordination shell and (filled circles) second coordination shell; (c) the Fourier transform magnitude spectra of the longer k range data, including (dashed green) raw data, (solid red) first Pt–Pt coordination shell and (filled circles) second coordination shell; (d) the filtered back-Fourier transform $k^1 \cdot \chi(k)$ versus k data over the shortened range of the (solid red) first Pt–Pt coordination shell and (filled circles) second Pt–Pt coordination shell; and (e) the corresponding Fourier transform magnitude spectra of the shortened k -range data, including (solid red) first Pt–Pt coordination shell and (filled circles) second Pt–Pt coordination shell. (For interpretation of the references to color in this figure legend, the reader is referred to the web version of this article.)

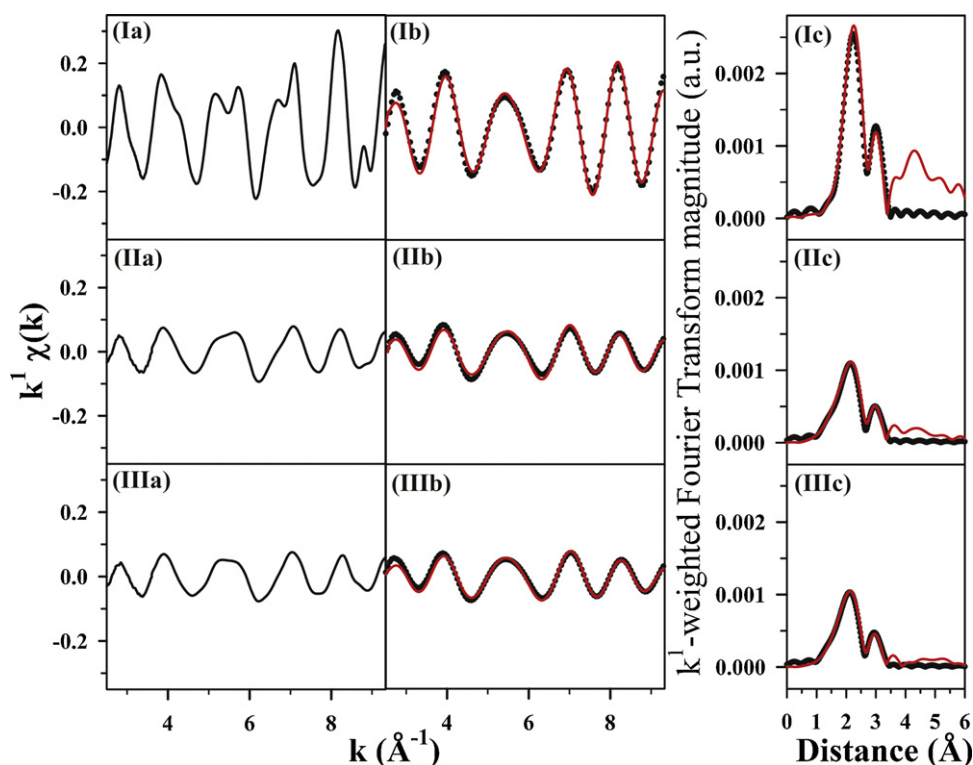


Fig. 4. EXAFS spectra of (a) raw $k^1 \cdot \chi(k)$ versus k spectra, (b) (solid red) filtered and (filled circles) fitted $k^1 \cdot \chi(k)$ versus k spectra, and (c) (solid red) raw and (filled circles) fitted phase-uncorrected Fourier transform magnitude spectra of (I) Pt⁰ foil, (II) H₂-reduced PBA and (III) H₂-reduced PBCA. (For interpretation of the references to color in this figure legend, the reader is referred to the web version of this article.)

Table 5
Summary of XPS data for prepared catalysts.^{a,b}

Catalyst	Atomic concentration (%)				Atomic ratio				
	Pt	Ba	Ce	Al	Pt/Ba	Pt/Ce	Pt/Al	Ba/Ce	Ba/Al
PBA	0.22	1.03	–	29.68	2.14	–	0.74	–	3.47
PBC	1.04	3.01	12.35	–	3.47	8.45	–	24.4	–
PCA	0.18	–	1.25	32.71	–	3.65	0.56	–	–
PBCA	0.24	1.51	0.83	32.12	1.58	7.2	0.74	45.7	4.61

^a Atomic sensitivity factors taken from Ref. [48].

^b The denominator of the atomic ratio was corrected to 100 wt%.

Finally, for PBCA, STEM measurements show the Al_2O_3 nanorods to be well dispersed and mixed with CeO_2 nanocrystals with different crystal dimensions (rod-shaped Al_2O_3 vs. prismatic CeO_2). The much greater atomic weight of cerium compared to aluminum leads to a speckled appearance in the STEM image of Fig. 7, where the prismatic CeO_2 crystals stand out as distinctly white spots on a gray background made up of Al_2O_3 nanorods. Characteristic larger grained clusters of BaO can be observed as isolated zones on top of the Al_2O_3 – CeO_2 support and are circled in the STEM image. The BaO clusters were analyzed using the X-ray detector and a corresponding spectrum with Ba peaks is included as an inset in Fig. 7. At greater magnification the HR-STEM image identifies Pt nanoparticles on the surfaces of the CeO_2 prismatic crystals and to a lesser extent on Al_2O_3 rods. The Pt-grains are on the order of 1–5 nm in diameter and the larger Pt grains are typically composed of several smaller individual Pt crystals as shown in the HR-STEM inset in Fig. 7. From the analyzed regions it is difficult to distinguish if any Pt grains are structurally associated with BaO or if

they are hosted by $\text{CeO}_2/\text{Al}_2\text{O}_3$ and merely coated by BaO clusters.

The reducibility of PCA, PBA, PBC and PBCA was studied by H_2 -TPR, the results of which are shown in Fig. 8. For comparison, the H_2 -TPR profiles of Pt/ CeO_2 (PC) and Pt/ Al_2O_3 (PA) were also recorded (see inset of Fig. 8). The main reduction features observed in the TPR profiles can be summarized as follows:

- (i) Reduction of PtO_x dispersed on CeO_2 : The TPR profile of PC shows two major reduction peaks at 250 °C and 470 °C. Comparing it with the profile for unpromoted CeO_2 , the lower temperature peak can be ascribed to the reduction of surface oxygen species. This phenomenon is attributed to reduction of the Pt, which is able to promote reduction of the surface CeO_2 via spillover of H atoms onto the support [35]. This peak was also observed over the PBC sample. The peak at 470 °C can be attributed to the reduction of bulk ceria. However, when

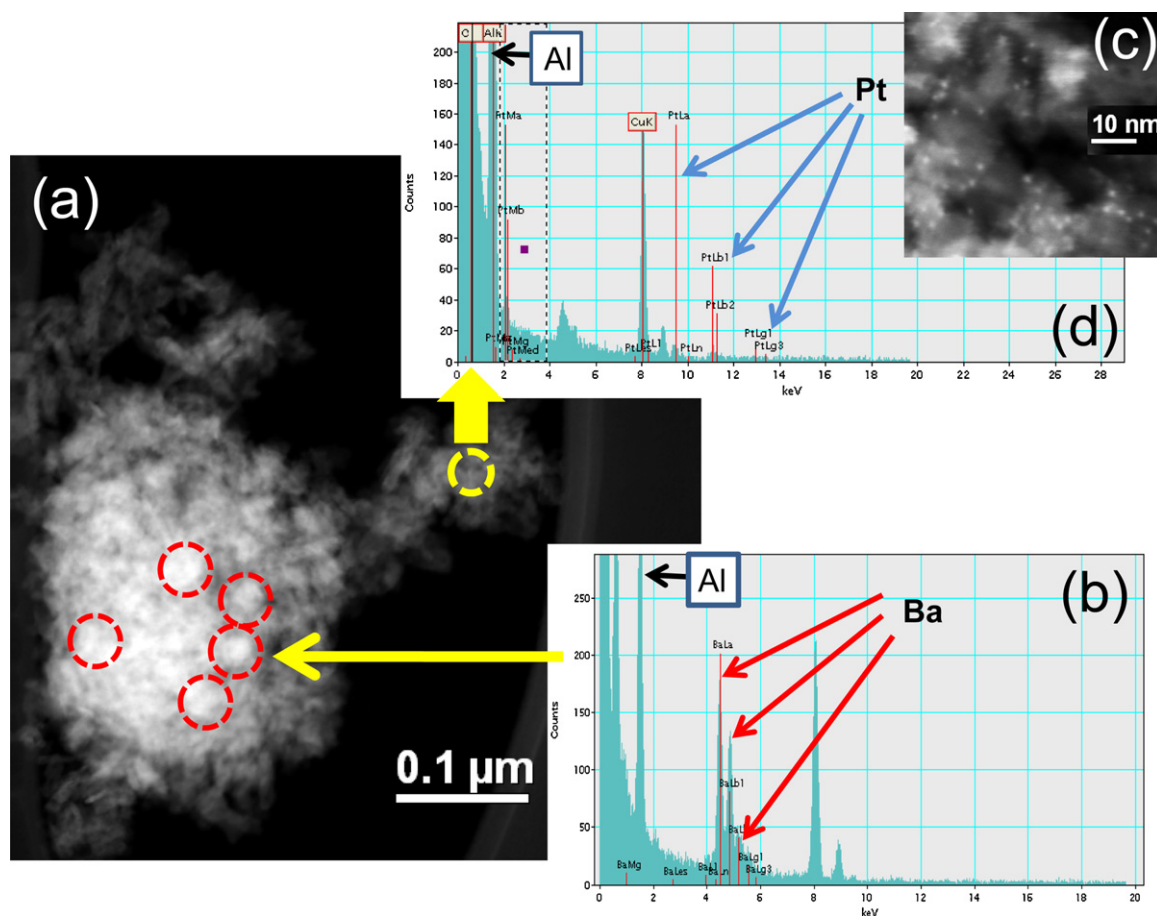


Fig. 5. (a) STEM image for PBA showing Al_2O_3 support and Ba-rich clusters; (b) EDX spectrum for circled area in (a); (c) EDX spectrum for area indicated in (a); (d) magnified image of area in (a) showing Pt nanoparticles. (For interpretation of the references to color in the text, the reader is referred to the web version of this article.)

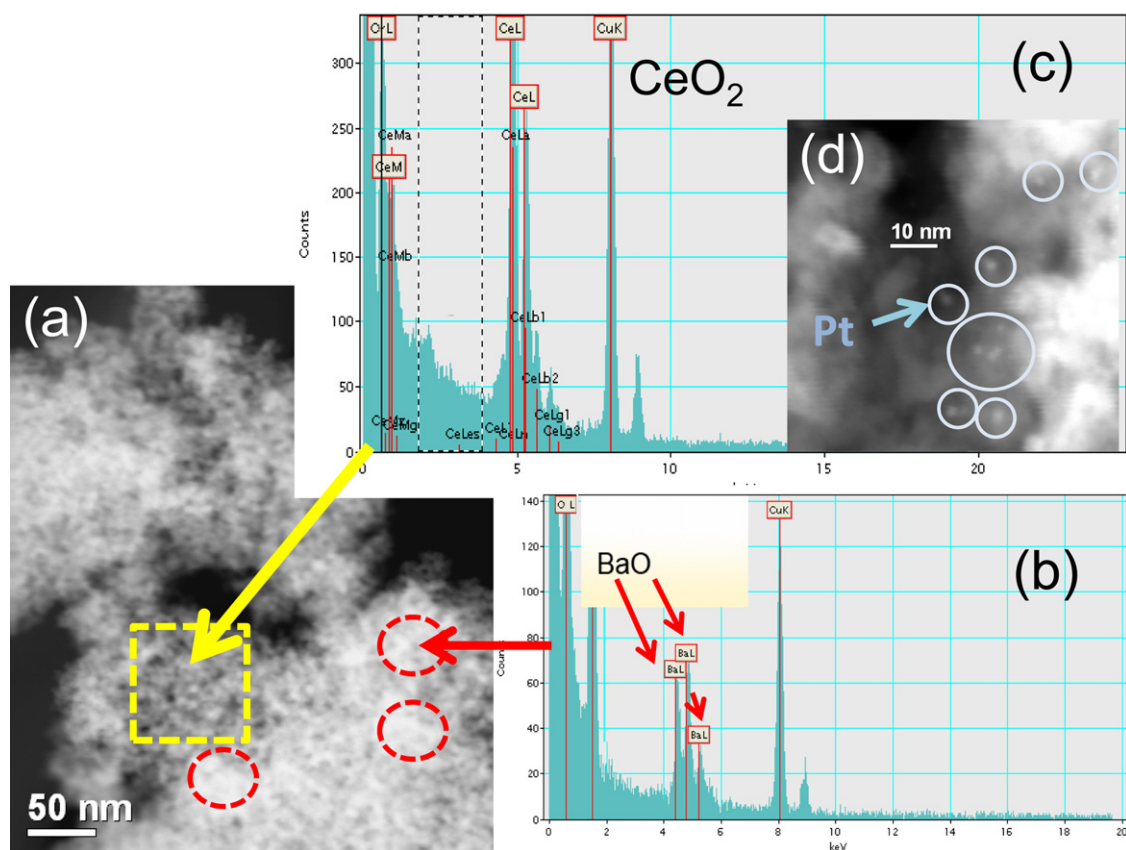


Fig. 6. (a) STEM image for PBC; (b) EDX spectrum for circled area in (a) showing presence of Ba; (c) EDX spectrum for boxed area in (a); (d) STEM image of Pt nanoparticles.

CeO₂ was loaded on γ -Al₂O₃, as for PCA and PBCA samples, the temperature maximum for the combined reduction of Pt and Ce surface species was further lowered from 250 °C to 205 °C. Tiernan and Finlayson [36] similarly reported slightly different temperatures for reduction of the surface species in Pt/CeO₂ (235–265 °C) and Pt/CeO₂/Al₂O₃ (220–250 °C).

(ii) Reduction of PtO_x dispersed on Al₂O₃: Two reduction peaks are observed for the PA sample at 205 °C and ca. 440 °C. The presence of two reduction peaks has on occasions been noted in the literature, although their assignment is not entirely straight forward [37,38]. In general, the low temperature peak is assigned to PtO₂ particles which interact weakly with the

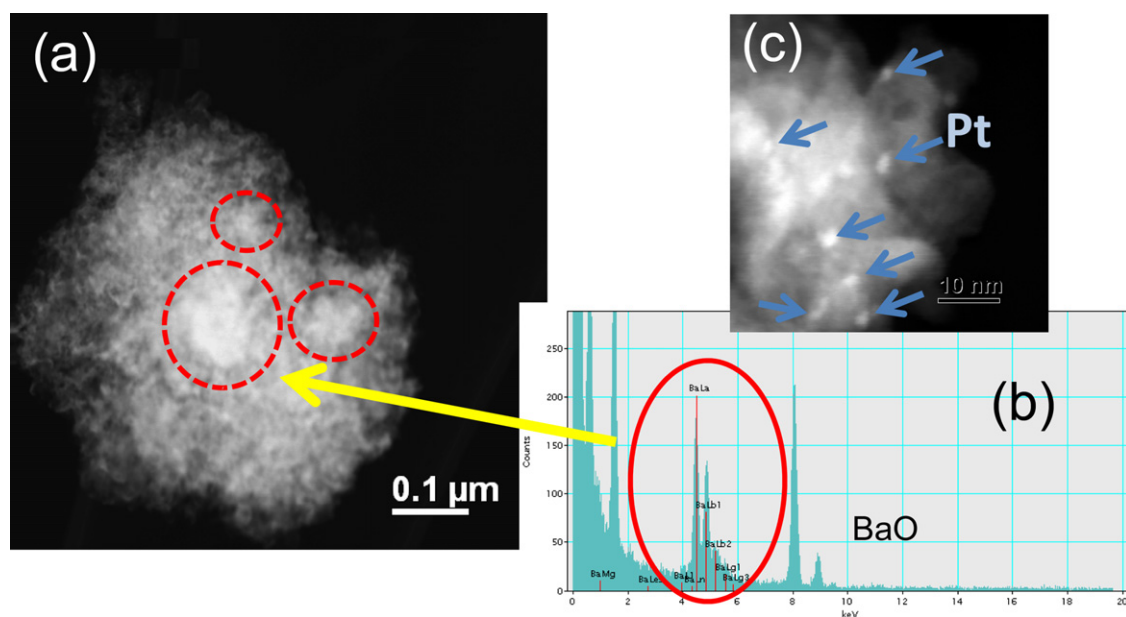


Fig. 7. (a) STEM image for PBCA; (b) EDX spectrum for circled area in (a) showing presence of Ba; (c) STEM image showing presence of Pt nanoparticles on CeO₂/Al₂O₃ support.

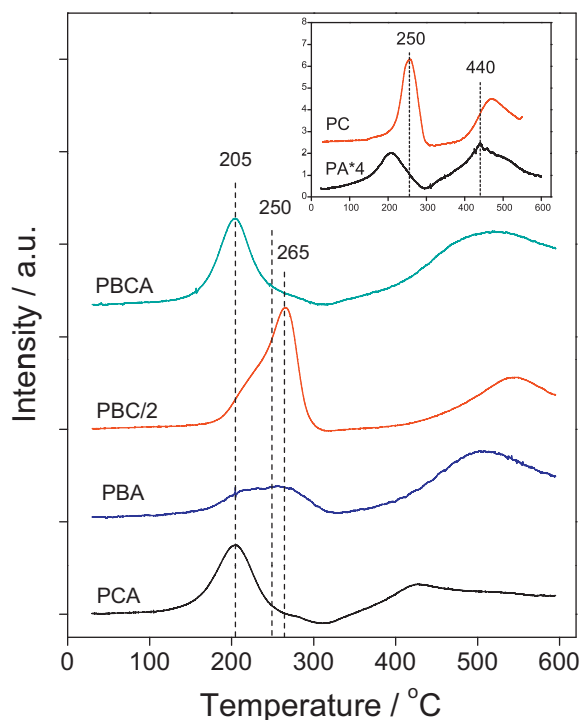


Fig. 8. H_2 -TPR profiles of PC, PA, PCA, PBA, PBC and PBCA samples obtained in 5% H_2/Ar . See Section 2.2 for experimental details.

support [39]. Most authors assign the high temperature peak to either Cl-containing Pt species such as PtO_xCl_y (when H_2PtCl_6 is used as the Pt precursor or when chloride is present as an impurity in the Pt salt used), or to highly dispersed PtO_x species which interact strongly with the alumina support [36,38,40]. In the present work, the presence of PtO_xCl_y was ruled out based on elemental analysis data. In addition, mass spectrometric analysis of the gases evolved during TPR revealed the absence of CO or CO_2 , thereby ruling out decomposition of carbonates on the support as a cause of H_2 consumption via the reverse water–gas shift reaction. Moreover, upon pre-treatment of sample PA, involving reduction under H_2 at 500 °C followed by oxidation at 500 °C, the TPR peak at 440 °C remained almost unchanged, suggesting that the peak is indeed associated with Pt which interacts strongly with the support.

- (iii) Similar to PA, a low temperature reduction peak at ca. 205 °C could be observed for PCA, PBA and PBCA. This observation is consistent with TEM data for catalyst PBA which suggests that Pt resides mostly on the alumina support, while for PBCA Pt resides mainly on the exposed CeO_2 and Al_2O_3 phases. A high temperature reduction peak is also evident at 440 °C for PCA (as observed for PA) and at ca. 510 °C for PBA and PBCA. In the case of PBA and PBCA, the high temperature peak is not associated with reduction of Pt since XAS data show that the Pt in both catalysts is almost completely reduced after treatment in H_2 at 300 °C. Indeed, as evidenced in Fig. 2, comparison of the near edge XAS spectra indicates that PBA and PBCA have similar white line intensity to the Pt foil reference. Instead, the high temperature reduction peak is most likely associated with the supported Ba, given that 10 wt% Ba/Al_2O_3 showed a broad reduction peak centered at 600 °C (data not shown), associated with either reduction of BaO_2 and/or the decomposition of $BaCO_3$, the liberated CO_2 consuming H_2 via the reverse water–gas shift reaction. In the presence of Pt, this peak shifts to lower temperature (~ 500 –520 °C).

- (iv) Reduction of PtO_x associated with BaO: Comparing the TPR profiles of PA and PBA, it is reasonable to ascribe the peak at 265 °C for PBA to H_2 -reduction of PtO_x interacting with BaO. Accordingly, this peak is also observed for the PBC and PBCA samples.

3.2. NO_x storage capacity

The NO_x storage capacities (NSCs) of the catalysts were measured at 200, 300 and 400 °C using a continuously flowing $NO + O_2$ mixture which also contained H_2O and CO_2 . The results for storage times of 2 min and 60 min are reported in Table 6. For the data collected at 2 min (which are of the most relevance to “real-world” lean-rich cycling conditions), the NSC values span a relatively narrow range, as might be expected given that the catalysts are far from saturation at this relatively short storage time. However, several trends are apparent, namely that: (i) catalyst PBC displays superior NSC to the other catalysts at all temperatures (particularly at 200 and 300 °C); (ii) all of the catalysts reach their maximum NSC at 300 °C, except for PBA which reaches its maximum at 400 °C; and (iii) PCA (containing no Ba) shows the lowest NSC of all the samples at 400 °C. Turning to the 60 min data, it is evident that many of the same trends hold. Indeed, PBA exhibits its highest NSC value of $287 \mu mol g^{-1}$ at 400 °C, which can be attributed to the fact that the strong surface basicity of BaO imparts relatively high thermal stability to the nitrate. In contrast, each of the Ce-containing samples (PBC, PCA and PBCA) displays their highest NSC at 300 °C. Again, the highest NSC value at 200 °C and 300 °C is obtained with PBC, indicating that the presence of ceria and barium as NO_x storage components significantly improved NO_x storage capacity at low and intermediate temperatures, in agreement with our previous findings [24]. The lowest NSC (at all temperatures) is shown by catalyst PCA, containing no barium, its poor performance at 400 °C being explained by the poor thermal stability of cerium nitrates [23,24].

3.3. Reduction of stored NO_x

The reduction of stored NO_x was investigated by means of TPR experiments in a gas mixture containing 4000 ppm H_2 , 5% CO_2 , 1% H_2O and balance He. The results are shown in Fig. 9. For PBA, an obvious H_2 consumption peak accompanied by N_2 ($m/e = 14$) and NH_3 ($m/e = 15$) formation was observed at 220 °C. The signal corresponding to $m/e = 14$ was used to detect N_2 instead of $m/e = 28$, since CO_2 ($m/e = 44$) also has a contribution ($>10\%$) for $m/e = 28$. Similarly, to avoid interference from H_2O ($m/e = 18$), NH_3 was detected using the signal at $m/e = 15$. In addition, changes were observed to the signal corresponding to $m/e = 30$. This signal can be attributed either to NO_x released during the reduction or to fragmentation of N_2O ($m/e = 44$) formed as a reduction product. From the data in Fig. 9, it is apparent that the surface nitrates on barium reacted with H_2 at low temperatures, H_2 consumption peaking at 210 °C for PBA with the simultaneous formation of N_2 , NH_3 and N_2O . The continuous H_2 consumption observed at higher temperatures (>300 °C) can be attributed to the reverse water–gas shift reaction.

In the case of PBC, the main H_2 consumption peak was observed at 100 °C, with a shoulder at ca. 210 °C. Significantly, the signal maxima corresponding to the evolution of N_2 , N_2O and NH_3 did not line up with the maximum observed for H_2 consumption, the maxima for the reduction products being observed at 120 °C, with a shoulder at 210 °C. These observations are consistent with reduction of the ceria in PBC preceding reduction of the nitrates stored on the ceria. This is also the case for sample PCA, reduction of the ceria resulting in a well defined H_2 consumption maximum at 60 °C, which was followed by the release of NO_x reduction products which reached their peak concentrations at ca. 100 °C.

Table 6NO_x storage capacity measured under lean conditions (300 ppm NO, 8% O₂, 5% CO₂, 1% H₂O, Ar balance, GHSV = 30,000 h⁻¹, storage time as indicated).

Catalyst code	NO _x storage capacity (μmol g ⁻¹)					
	200 °C/2 min	300 °C/2 min	400 °C/2 min	200 °C/60 min	300 °C/60 min	400 °C/60 min
PBA	18	18	20	160	269	287
PBC	21	22	21	268	386	303
PCA	16	20	14	90	233	195
PBCA	16	18	16	247	370	341

Upon raising the NO_x adsorption temperature from 200 °C to 360 °C, the H₂ consumption profile of PBC changed considerably. Specifically, the reduction peak at 210 °C became larger, corresponding to increased H₂ consumption, with increased N₂, N₂O, and NH₃ formation at this temperature. As is apparent from the NO_x storage capacities shown in Table 6, the stronger basicity of BaO in comparison with CeO₂ favors NO_x storage on the BaO phase at high temperatures. The finding that the NO_x reduction peak at 210 °C became stronger when the adsorption temperature was raised to 360 °C confirms that the reduction peak at 210 °C is due to H₂-reduction of nitrates adsorbed on BaO, while that at 120 °C is associated with the reduction of nitrates on CeO₂. These assignments are also consistent with the TPR profile obtained with PBA.

Turning to NO_x reduction over PBCA, two well resolved reduction peaks were observed at 120 °C and 210 °C, which can be assigned to the H₂-reduction of nitrates stored on CeO₂ and on BaO, respectively.

3.4. Cycling experiments

NO_x storage and reduction were also investigated under cycling conditions, the NO_x concentration profiles being shown in Fig. 10. The corresponding cycle-averaged NO_x conversions are collected in Table 7. Note that NO_x conversion refers to the conversion of NO_x to reduction products, i.e., N₂, NH₃ and N₂O. At 200 °C, the Ce-containing samples showed improved NO_x conversions compared with PBA, consistent with the beneficial effects of cerium on NO_x storage and reduction at low temperatures. Increase of the temperature from 200 °C to 300 °C resulted in increased NO_x conversions, the NO_x conversion obtained over PBCA reaching 100%. Further increase in the temperature to 400 °C resulted in decreased NO_x conversions, except for PBA.

Catalyst performance during the lean phase can be evaluated in terms of the NO_x storage efficiency (NSE), defined as the amount of NO_x stored divided by the total amount of NO_x supplied to the catalyst during the lean phase. Comparing the NSE for the four samples (Table 7), it is clear that CeO₂ promotes NO_x storage at low temperatures. Indeed, at 200 °C the NSE values for the ceria-containing samples are between 44% and 113% (relative) higher than that of PBA. In contrast, each of the ceria-containing samples showed decreased NSE values upon increasing the temperature from 300 to 400 °C, while the NSE determined for PBA reached its highest value of 88.2% at 400 °C. This again serves to emphasize that BaO is beneficial for NO_x storage at higher temperatures, a fact which can be attributed to the stronger basicity of Ba compared to Ce, and hence the superior thermal stability of Ba nitrates relative to Ce nitrates [23,24].

Rich phase performance can be characterized in terms of the percentage of NO_x released, i.e., the amount of NO_x released during the rich phase divided by the total amount of NO_x stored during the lean phase. Rich phase NO_x release is dependent on the rates of four processes as highlighted by Epling et al. [41]: reductant delivery, nitrate decomposition, consumption of stored oxygen and NO_x reduction. From this, it follows that for a given set of conditions it is important to establish a balance between nitrate decomposition and NO_x reduction. In this study, for each sample the

lowest NO_x release percentage was observed at 300 °C. The comparatively higher NO_x release at 200 °C can be ascribed to an imbalance between the rates of nitrate decomposition and NO_x reduction, i.e., the rate of NO_x reduction was too slow for the liberated NO_x to be fully consumed. At 400 °C, the thermal instability of the nitrates was such that the rate of nitrate decomposition was also much higher than that of NO_x reduction (even though the latter should be fast at this temperature), resulting in significant NO_x slip. The intermediate temperature of 300 °C therefore represents an optimum at which a balance is achieved between the rates of nitrate decomposition and NO_x reduction.

4. Discussion

In this study Ce-containing LNT catalysts were prepared for comparison with a “first-generation” catalyst of the Pt/BaO/Al₂O₃ type. Considering first the micro-structure of the ceria-based LNT catalysts, H₂ chemisorption, STEM and EXAFS data showed that Pt in the catalysts was in each case highly dispersed. According to XRD data, the dispersion of crystalline BaCO₃ in the catalysts followed the order PBCA > PBC > PBA. STEM measurements also suggest that for each catalyst the Pt is located mainly on the support material, rather than on the Ba phase itself.

From H₂-TPR results shown in Fig. 8, it is evident that three main types of PtO_x species are present in the various catalysts corresponding to: (i) PtO_x associated with BaO, which gives rise to a H₂-reduction peak at 260 °C; (ii) PtO_x on CeO₂, which displays a reduction peak at or near 205 °C, the exact temperature being impossible to discern due to the simultaneous reduction of surface ceria; (iii) Pt on γ-Al₂O₃, which exhibits a reduction peak at the much higher temperature of 440 °C. These results clearly indicate that loading Pt on different supports modifies its redox properties. Specifically, PtO_x supported on CeO₂ can be reduced at a lower temperature than PtO_x which is associated with BaO. Based solely on H₂-TPR data, it is difficult to discriminate quantitatively between Pt supported on cerium, baria and alumina, due to the reduction of CeO₂ itself. However, it is apparent that Pt is preferentially dispersed on the γ-Al₂O₃ phase in catalyst PBA, since the peak due to Pt reduction on γ-Al₂O₃ is much stronger than the reduction peak due to PtO_x/BaO. STEM observations also support this conclusion. This finding is to be expected given that γ-Al₂O₃ has much larger surface area than the BaO phase. However, for efficient LNT functioning, it is crucial that the Pt and NO_x storage sites are in close proximity, as shown by a number of recent studies [7,8]. In this respect, it should be advantageous to support all of the Pt on the NO_x storage materials in the catalyst (as for PBC), such that all of the Pt can in principle participate in NO_x storage and reduction (providing the operating temperature falls in the range in which ceria is able to store NO_x), as opposed to the situation in PBA in which only a limited fraction of the Pt is in direct contact with the NO_x storage phase.

NO_x storage capacity is an important parameter for the evaluation of a LNT catalyst, since a high NSC, when coupled with adequate regeneration, implies good lean phase performance. As shown in Table 6, the use of CeO₂ as support for the BaO phase (in PBC), provides the highest NSC. This is easy to understand in that both BaO

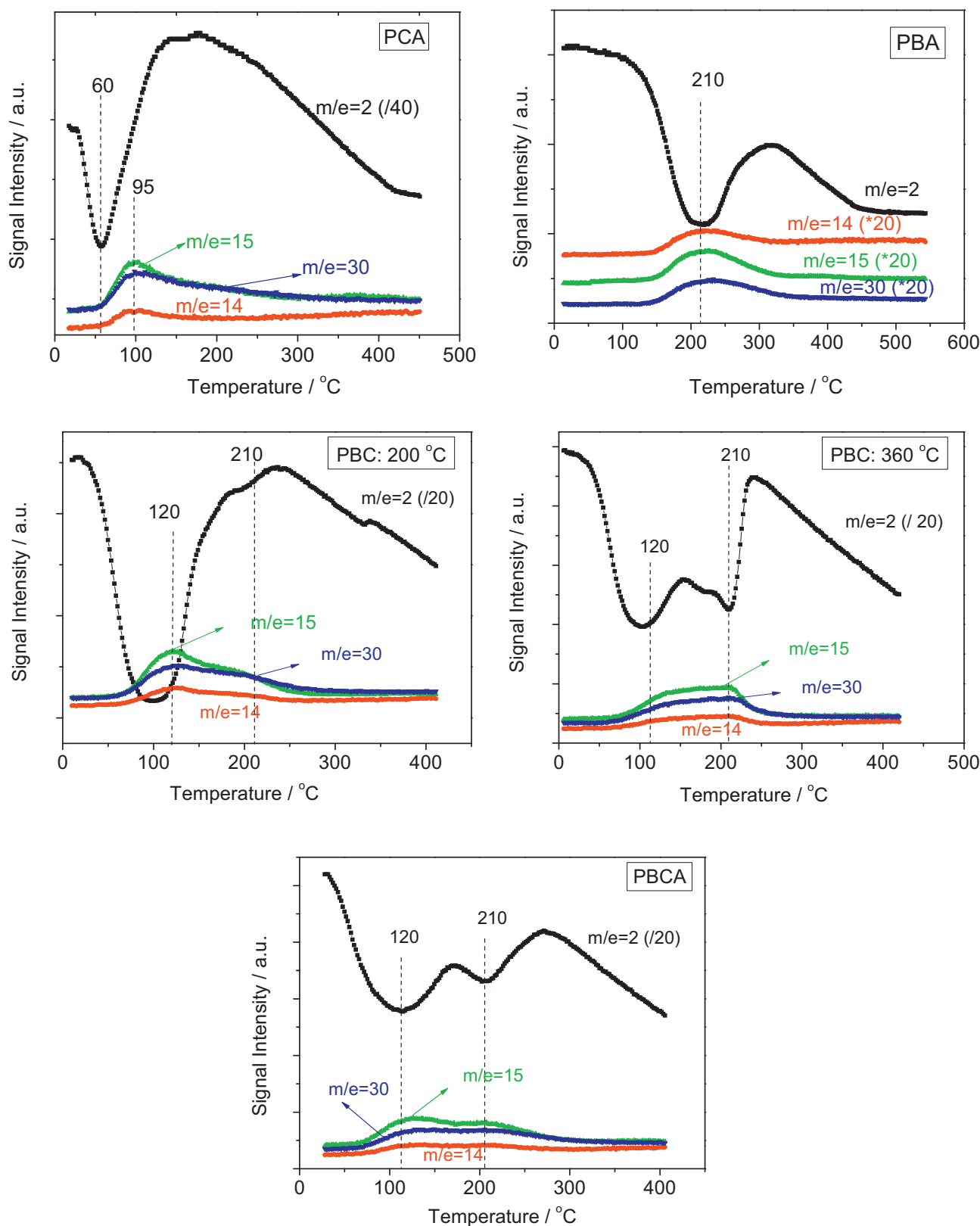


Fig. 9. TPR profiles in 0.4% H₂/5% CO₂/5% H₂O/He after NO adsorption using 300 ppm NO/8% O₂/5% CO₂/1% H₂O/He for 1 h; NO adsorption was performed at 200 °C unless otherwise stated.

and CeO₂ exhibit NO_x storage capacity. In contrast, when CeO₂ is present as the only NO_x storage component (as for catalyst PCA), the NSC is the poorest at all temperatures. This can be attributed to the much weaker basicity of CeO₂ compared with BaO, the latter

representing a strong solid base [42]. In the case of PBCA, the NSC at 200 and 300 °C is lower than that measured for PBC, but higher than for PBA. These results indicate that although CeO₂ itself can store NO_x, the coupling of CeO₂ with BaO affords optimal NSC. We

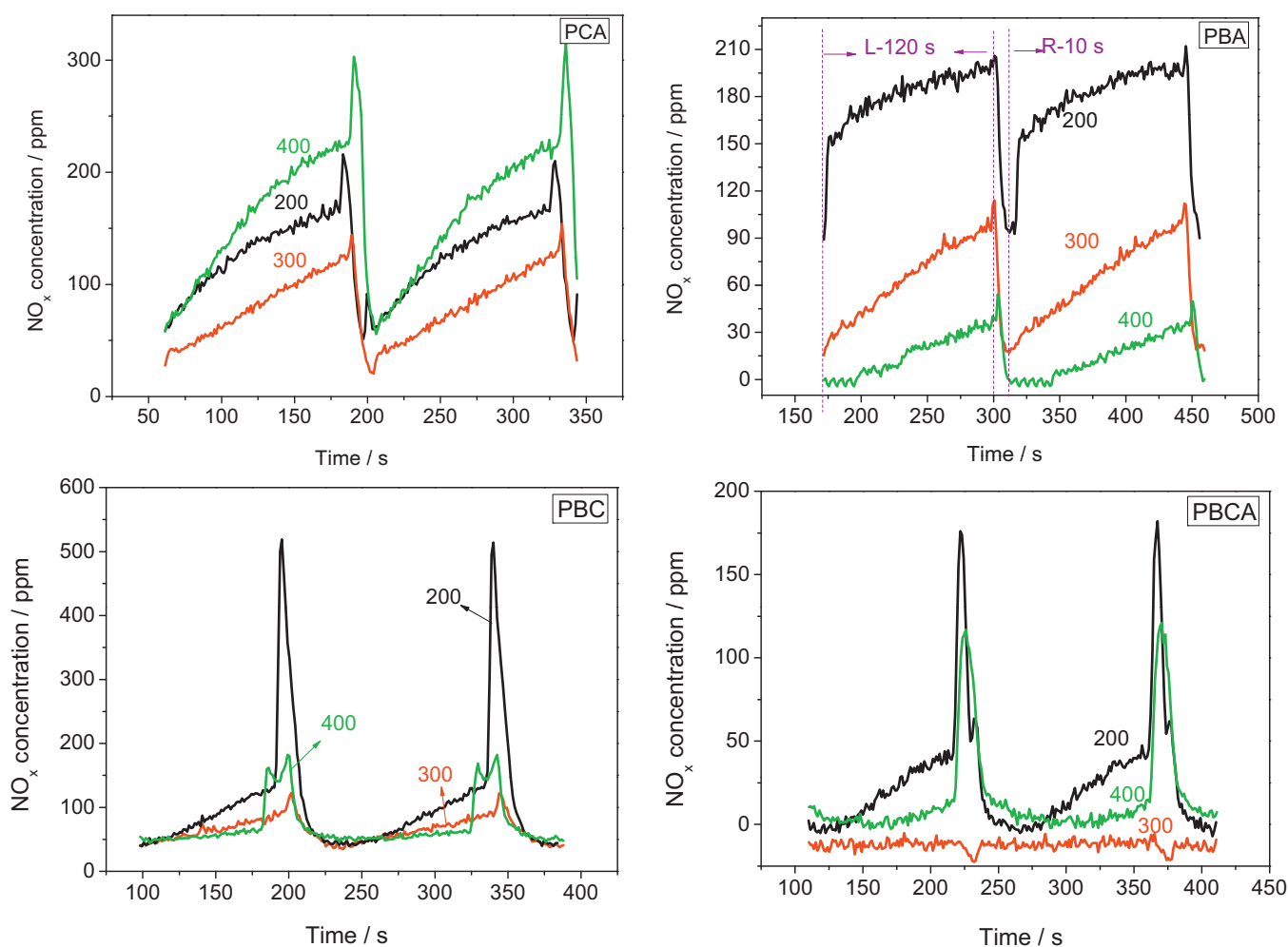


Fig. 10. NO_x concentration profiles during lean-rich cycling at 200, 300 and 400 °C. See Table 2 for experimental conditions.

suggest that this may be a consequence of the higher (crystalline) BaCO_3 dispersions in the ceria-containing catalysts relative to PBA, in addition to the ability of CeO_2 itself to store NO_x . As indicated above, the NO_x storage and reduction performance of LNT catalysts is strongly dependent on the degree of Pt–Ba contact, this being a function of the dispersions of these two components. Higher dispersions result in increased contact, as reflected in the interfacial perimeter [43,44], and hence in improved NO_x storage and reduction. It is also noteworthy that all of the Ce-containing catalysts show better NSC at 200 °C compared with PBA, which agrees with

the results from our previous studies [24], and which is consistent with the role of ceria in NO_x storage at low temperatures.

The reduction of stored NO_x plays a crucial role in the functioning of LNT catalysts – if a catalyst cannot be regenerated during the rich phase, it cannot store NO_x during the subsequent lean phase. According to the TPR results shown in Fig. 9, NO_x adsorbed on BaO in PBA, PBC and PBCA was reduced at 210 °C, whereas NO_x stored on CeO_2 was reduced at the lower temperature of 120 °C. This provides a clear indication that the presence of CeO_2 is beneficial for low temperature regeneration performance. From Fig. 9 it is apparent that

Table 7
Comparison of NO_x storage and release during NO_x storage/reduction cycling.

Temperature (°C)	Catalyst	NO_x conversion (%)	NO_x storage efficiency (%)	Rich phase NO_x release (%) ^a
200	PBA	30.1	36.6	6.1
	PBC	55.5	67.6	12.1
	PCA	46.8	52.8	6.1
	PBCA	72.3	78.0	5.9
300	PBA	66.8	70.7	3.9
	PBC	68.3	72.7	4.3
	PCA	61.1	65.5	4.4
	PBCA	100	100	0
400	PBA	80.3	88.2	8
	PBC	67.7	74.9	7.2
	PCA	34.7	42.4	7.8
	PBCA	76.8	81.2	4.4

^a (NO_x released in rich purge/ NO_x stored in lean phase) \times 100%.

reduction of the NO_x species adsorbed on CeO_2 is immediately preceded by the reduction of the CeO_2 surface. Close examination of the TPR profiles reveals that evolution of the NO_x reduction products commences at the same temperature at which the H_2 consumption reaches a maximum (PCA) or slightly before it (PBC, PBCA). This suggests that reduction of the adsorbed NO_x is initiated by the reduction of the surface Ce^{4+} sites in the ceria phase, i.e., reduction of the ceria surface effectively destabilizes the surface nitrates, resulting in NO_x release and its subsequent reduction.

Our data also show that the presence of stored NO_x in the ceria-containing catalysts exerts a significant effect on the ceria reduction temperature. Whereas reduction occurs in the temperature range 205–250 °C in the absence of NO_x (Section 2.1), after NO_x storage this temperature is decreased to 60–100 °C. The latter observation is consistent with our previous study [24], in which the onset of ceria reduction was observed at 80 °C for a catalyst consisting of a physical mixture of $\text{Pt/BaO/Al}_2\text{O}_3 + \text{Pt/CeO}_2$ which had been similarly loaded with NO_x . Given that Pt reduction has to occur prior to ceria reduction (in order to facilitate hydrogen spillover onto the ceria surface), one possible explanation for these observations is that the presence of surface nitrates weakens the Pt– CeO_2 interaction. Based on EXAFS data, this interaction has been characterized in terms of Pt–O–Ce linkages [45]. If the presence of nitrates were to interrupt this bonding, then it can be anticipated that the reduction temperature of the weakly interacting PtO_x clusters would be shifted towards lower temperatures, and thereby the ceria reduction temperature. However, additional work is needed to prove or disprove this hypothesis.

Turning to the lean-rich cycling data, PCA displayed the lowest activity for NO_x conversion, which is explained by its poor NO_x storage efficiency. In the case of PBC, its comparatively high NSE (shown in Table 7), results in better NO_x conversion at 200 and 300 °C compared with PCA and PBA. Overall, catalyst PBCA showed the best performance over the range 200–400 °C; NO_x conversions were in excess of 75% throughout the whole temperature range, reaching 100% at 300 °C.

It is important to note that there are two factors that determine the NSE during lean-rich cycling: one is the “intrinsic” storage efficiency, as measured by the static storage efficiency of the initially NO_x -free catalyst (in this case for 2 min); and the other is the extent to which NO_x storage sites are regenerated during rich purging. Although nitrates were reduced in the rich phase at temperatures lower than 200 °C according to TPR data (Fig. 9), at low temperatures NO_x release may be kinetically limited under lean-rich cycling conditions due to the relatively short rich phase. Hence, at 200 °C NSE may be limited by either incomplete regeneration of the storage sites or by the kinetics of NO oxidation to NO_2 during the NO_x storage phase (which can limit the NO_x capture efficiency). A comparison of the 2 min static storage capacities (Table 6) with the NSE's determined from the cycling data (also corresponding to a lean storage time of 2 min, see Table 7) is shown in Fig. 11. Considering the data collected at 200 °C, it is apparent that the ceria-containing catalysts show better regeneration properties than PBA, the amount of NO_x stored for PBA during lean-rich cycling being slightly less than half that stored under static (i.e., continuous lean flow) conditions. This is in broad agreement with our previous studies [24,25], in which it was observed that catalyst regeneration behavior was improved by the addition of Pt/CeO_2 to $\text{Pt/BaO/Al}_2\text{O}_3$ (as a physical mixture), particularly at low temperatures. Remarkably, for PBCA the same amount of NO_x is stored under both conditions, suggesting that the catalyst is fully regenerated during cycling (although the comparison may not be completely valid, as discussed below). In contrast, at 300 and 400 °C the regeneration of PBA is more efficient than that of PBC and PCA, the amount of NO_x stored during cycling, relative to that stored under static conditions, being greater for PBA. That said, the

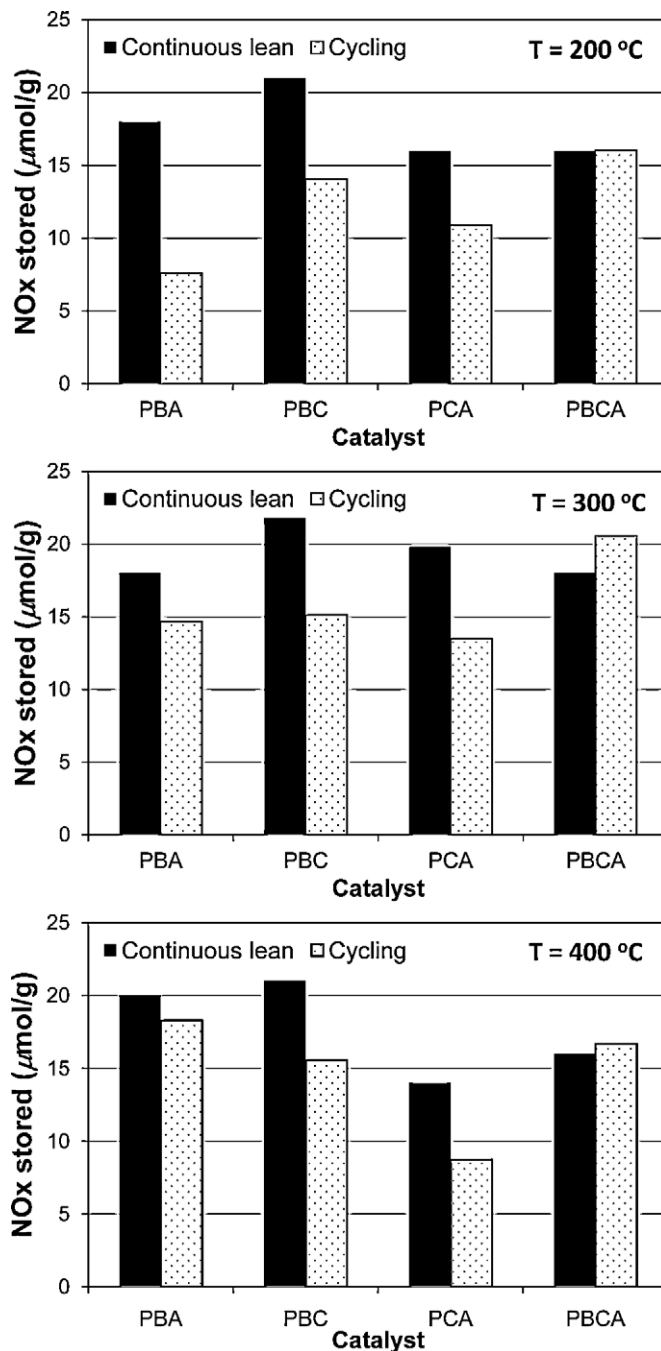


Fig. 11. Comparison of 2 min static NO_x storage capacities and 2 min NO_x storage efficiencies under lean-rich cycling. See Section 2.4 and Table 2, respectively, for experimental conditions.

absolute amount of NO_x stored during cycling is still slightly greater at 300 °C for PBC than PBA, due to the higher intrinsic NSC of the former. At 400 °C PBA shows the highest amount of NO_x stored during cycling, this being a consequence of its high intrinsic NSC at this temperature, coupled with its good high temperature regeneration properties.

Comparing the catalysts, it is evident that PBCA possesses the best regeneration properties at all three temperatures. Remarkably, the amount of NO_x stored by PBCA during cycling at 300 and 400 °C is found to be slightly higher than that stored under static conditions. These results are hard to reconcile, although a likely explanation for this apparent anomaly is that the initial state of the catalyst in the two sets of measurements was different. For

example, the process of repeated NO_x storage and reduction during cycling may have displaced carbonate from Ba-based storage sites, thereby “freeing up” sites for NO_x storage. Indeed, we have previously observed that complete removal of carbonate species requires the use of NO_x storage–reduction (cycling) conditions (albeit in the absence of CO₂ [46], which is not the case here), whereas high temperature treatments under H₂ (as used for the pre-treatment prior to both static and cycling experiments) typically leave a small amount of carbonate remaining on the surface. Consequently, more NO_x storage sites would be available under the cycling conditions relative to the static experiment. An alternative explanation is that re-dispersion of the Ba phase may have occurred during cycling (bearing in mind that typically 2 h of cycling was performed between measurements in order to ensure “stationary” cycles were attained), resulting in increased storage capacity. Consequently, the data in Fig. 11 must be treated with caution.

At this juncture it should be noted that based on their work with model catalysts, Le Phuc et al. [47] have inferred that the high catalytic activity of ceria for the reduction of NO_x with NH₃ can explain the increased NO_x conversion levels and decreased NH₃ emissions obtained with ceria-containing catalysts. However, this finding does not in itself explain the superior regeneration properties of PBC and PBCA noted above, i.e., the fact that NO_x is more readily released under rich conditions. Alternative explanations must therefore be sought, of which two are apparent. First, the fact that reductive nitrate decomposition is observed to be a more facile process on ceria than on baria, should result in improved regeneration kinetics for ceria-containing catalysts at low temperatures. Second, if Ba dispersions are indeed higher in the ceria-containing catalysts, then this should be advantageous with respect to catalyst regeneration. Specifically, during reverse spillover, improved Pt–Ba contact results in decreased kinetic limitations with respect to the solid state diffusion of NO_x within the Ba phase [43]. Consequently, catalyst regeneration behavior is improved, in addition to NSC.

Turning to a comparison of PBC and PBCA, the data in Table 7 again indicate that NSE is a decisive factor in explaining the better NO_x conversion of PBCA. The NSE of PBCA is superior to that of PBC, despite the fact that the two catalysts show similar NSC under static conditions. This indicates that PBCA can be more effectively regenerated under cycling conditions. This may be a consequence of the slightly smaller Ba particle size in PBCA (and hence better Pt–Ba contact) and/or the fact that PtO_x is easier to reduce on dispersed CeO₂ than on bulk CeO₂ according to the H₂–TPR results. This fact can also explain the relatively high percentage of NO_x that is released by PBC at 200 °C during cycling; given that PtO_x reduction must occur before NO_x desorbed from the storage materials can dissociatively adsorb on Pt and undergo reduction, if the kinetics of PtO_x reduction are slower for PBC than PBCA, then more NO_x can be expected to slip from the catalyst during the rich phase, as is indeed observed.

5. Conclusions

In this study the contribution of ceria to the NO_x storage and reduction properties of a series of model LNT catalysts was investigated. Lower H₂–reduction temperatures were observed for PtO_x supported on CeO₂ in comparison with PtO_x on BaO and γ-Al₂O₃, indicating the improved redox properties of the Ce-containing samples. Ceria-containing catalysts PBC and PBCA exhibited better NO_x storage capacity at 200 and 300 °C relative to the ceria-free PBA catalyst. Furthermore, regeneration behavior at low temperature was greatly improved by the presence of ceria. These factors contributed to the superior NO_x storage–reduction performance exhibited by catalysts PBC and PBCA under cycling conditions in the temperature range 200–300 °C. Overall, catalyst PBCA (which displayed

well balanced NO_x storage and regeneration behavior), showed the best performance, affording consistently high NO_x conversion levels (>75%) in the temperature range 200–400 °C.

Disclaimer

This report was prepared as an account of work sponsored by an agency of the United States Government. Neither the United States Government nor any agency thereof, nor any of their employees, makes any warranty, express or implied, or assumes any legal liability or responsibility for the accuracy, completeness, or usefulness of any information, apparatus, product, or process disclosed, or represents that its use would not infringe privately owned rights. References herein to any specific commercial product, process, or service by trade name, trademark, manufacturer, or otherwise does not necessarily constitute or imply its endorsement, recommendation, or favoring by the United States Government or any agency thereof. The views and opinions of authors expressed herein do not necessarily state or reflect those of the United States Government or any agency thereof.

Acknowledgments

Rhodia is thanked for a gift of CeO₂. This project was funded by the U.S. Department of Energy (DOE) under award No. DE-EE0000205.

References

- [1] C.H. Kim, G.S. Qi, K. Dahlberg, W. Li, *Science* 327 (2010) 1624.
- [2] M. Koebel, M. Elsener, M. Kleemann, *Catal. Today* 59 (2000) 335.
- [3] S. Roy, A. Baiker, *Chem. Rev.* 109 (2009) 4054.
- [4] N. Takahashi, H. Shinjoh, T. Iijima, T. Suzuki, K. Yamazaki, K. Yokota, H. Suzuki, N. Miyoshi, S. Matsumoto, T. Tanizawa, T. Tanaka, S. Tateishi, K. Kasahara, *Catal. Today* 27 (1996) 63.
- [5] K. Skalska, J.S. Miller, S. Ledakowicz, *Sci. Total Environ.* 408 (2010) 3976.
- [6] T. Johnson, *Platinum Met. Rev.* 52 (2008) 23.
- [7] N.W. Cant, I.O.Y. Liu, M.J. Patterson, *J. Catal.* 243 (2006) 309.
- [8] A. Kumar, M.P. Harold, V. Balakotaiah, *J. Catal.* 270 (2010) 214.
- [9] R. Monte, J. Kaspar, *Top. Catal.* 28 (2004) 47.
- [10] S. Bernal, G. Blanco, J.J. Calvino, J.M. Gatica, J.A.P. Omil, J.M. Pintado, *Top. Catal.* 28 (2004) 31.
- [11] M. Piacentini, M. Maciejewski, A. Baiker, *Appl. Catal. B* 72 (2007) 105.
- [12] A. Trovarelli, *Catal. Rev.* 38 (1996) 439.
- [13] M. Eberhardt, R. Riedel, U. Gobel, J. Theis, E.S. Lox, *Top. Catal.* 30–31 (2004) 135.
- [14] M. Casapu, J.D. Grunwaldt, M. Maciejewski, M. Wittrock, U. Göbel, A. Baiker, *Appl. Catal. B* 63 (2006) 232.
- [15] M. Casapu, J.D. Grunwaldt, M. Maciejewski, A. Baiker, M. Wittrock, U. Göbel, S. Eckhoff, *Top. Catal.* 42–43 (2007) 3.
- [16] M. Yang, Y. Li, J. Wang, M. Shen, *J. Catal.* 271 (2010) 228.
- [17] D.H. Kim, Y.-H. Chin, J.H. Kwak, J. Szanyi, C.H.F. Peden, *Catal. Lett.* 105 (2005) 259.
- [18] D.H. Kim, J.H. Kwak, J. Szanyi, S.D. Burton, C.H.F. Peden, *Appl. Catal. B* 72 (2007) 233.
- [19] M.O. Symalla, A. Drochner, H. Vogel, S. Philipp, U. Gobel, W. Muller, *Top. Catal.* 42–43 (2007) 199.
- [20] M. Haneda, T. Morita, Y. Nagao, Y. Kintaichi, H. Hamada, *Phys. Chem. Chem. Phys.* 3 (2001) 4696.
- [21] H.Y. Lin, C.J. Wu, Y.W. Chen, C.H. Lee, *Ind. Eng. Chem. Res.* 45 (2006) 134.
- [22] N. Le Phuc, E.C. Corbos, X. Courtois, F. Can, P. Marecot, D. Duprez, *Appl. Catal. B* 93 (2009) 12.
- [23] E. Rohart, V. Bellière-Baca, K. Yokota, V. Harlé, C. Pitois, *Top. Catal.* 42–43 (2007) 71.
- [24] Y. Ji, T.J. Toops, M. Crocker, *Catal. Lett.* 119 (2007) 257.
- [25] Y. Ji, J.S. Choi, T.J. Toops, M. Crocker, M. Naseri, *Catal. Today* 136 (2008) 146.
- [26] Y. Ji, C. Fisk, V. Easterling, U. Graham, A. Poole, M. Crocker, J.-S. Choi, W. Partridge, K. Wilson, *Catal. Today* 151 (2010) 362.
- [27] V. Easterling, Y. Ji, M. Crocker, J. Ura, J.R. Theis, R.W. McCabe, *Catal. Today* 151 (2010) 338.
- [28] J.H. Kwak, D.H. Kim, J. Szanyi, C.H.F. Peden, *Appl. Catal. B* 84 (2008) 545.
- [29] H. Mahzoul, L. Limousy, J.F. Brilhac, P. Gilot, *J. Anal. Appl. Pyrol.* 56 (2000) 179.
- [30] T. Ressler, *J. Synchrotron Radiat.* 5 (1998) 118.
- [31] B. Ravel, *J. Synchrotron Radiat.* 8 (2001) 314.
- [32] M. Newville, B. Ravel, D. Haskel, J.J. Rehr, E.A. Stern, Y. Yacoby, *Physica B* 208–209 (1995) 154.
- [33] J.T. Miller, B.L. Mojat, D.E. Ramaker, D.C. Koningsberger, *Catal. Today* 62 (2000) 101.

- [34] D.C. Koningsberger, D.E. Ramaker, J.T. Miller, J. De Graaf, B.L. Mojet, *Top. Catal.* 15 (2001) 35.
- [35] J. Kaspar, P. Fornasiero, M. Graziani, *Catal. Today* 50 (1999) 285.
- [36] M.J. Tiernan, O.E. Finlayson, *Appl. Catal. B* 19 (1998) 23.
- [37] C.-P. Hwang, C.-T. Yeh, *J. Mol. Catal. A* 112 (1996) 295.
- [38] T. Huizinga, J. Van Groundelle, R. Prins, *Appl. Catal. A* 10 (1984) 199.
- [39] H.C. Yao, M. Sieg, H.K. Plummer, *J. Catal.* 59 (1979) 365.
- [40] D. Gonzalez, E. Lima, N. Martin, *Ind. Eng. Chem. Res.* 46 (2007) 4335.
- [41] W.S. Epling, A. Yezerets, N.W. Currier, *Appl. Catal. B* 74 (2007) 117.
- [42] K. Tanabe, M. Misono, Y. Ono, H. Hattori, *New Solid Acids and Bases*, Stud. Surf. Sci. Catal., vol. 51, Elsevier, Amsterdam, 1989, pp. 16–21.
- [43] D. Bhatia, M.P. Harold, V. Balakotaiah, *Catal. Today* 151 (2010) 314.
- [44] Y. Ji, V. Easterling, U. Graham, C. Fisk, M. Crocker, J.-S. Choi, *Appl. Catal. B* 103 (2011) 413.
- [45] Y. Nagai, T. Hirabayashi, K. Dohmae, N. Takagi, T. Minami, H. Shinjoh, S. Matsumoto, *Catal. J.* 242 (2006) 103.
- [46] Y. Ji, T.J. Toops, J.A. Pihl, M. Crocker, *Appl. Catal. B* 91 (2009) 329.
- [47] N. Le Phuc, X. Courtois, F. Can, S. Royer, P. Marecot, D. Duprez, *Appl. Catal. B* 102 (2011) 362.
- [48] C.D. Wagner, in: D. Briggs, M.P. Seah (Eds.), *Practical Surface Analysis*, vol. 1, 2nd edition, J. Wiley and Sons, 1990.